Cell, Vol. 105, 473–485, May 18, 2001, Copyright ©2001 by Cell Press

Structural Biochemistry and Interaction Architecture of the DNA Double-Strand Break Repair Mre11 Nuclease and Rad50-ATPase

Karl-Peter Hopfner,[1,5] Annette Karcher,[1] Lisa Craig,[1] Tammy T. Woo,[1] James P. Carney,[3] and John A. Tainer[1,2,4]

[1] Department of Molecular Biology and Skaggs Institute for Chemical Biology
The Scripps Research Institute
La Jolla, California 92037
[2] Life Sciences Division
Lawrence Berkeley National Laboratory
Berkeley, California 94720
[3] The Radiation Oncology Research Laboratory
Department of Radiation Oncology
Marlene and Stewart Greenebaum Cancer Center and Molecular and Cell Biology Graduate Program
University of Maryland School of Medicine
Baltimore, Maryland 21201

Summary

To clarify functions of the Mre11/Rad50 (MR) complex in DNA double-strand break repair, we report *Pyrococcus furiosus* Mre11 crystal structures, revealing a protein phosphatase-like, dimanganese binding domain capped by a unique domain controlling active site access. These structures unify Mre11's multiple nuclease activities in a single endo/exonuclease mechanism and reveal eukaryotic macromolecular interaction sites by mapping human and yeast Mre11 mutations. Furthermore, the structure of the *P. furiosus* Rad50 ABC-ATPase with its adjacent coiled-coil defines a compact Mre11/Rad50-ATPase complex and suggests that Rad50-ATP-driven conformational switching directly controls the Mre11 exonuclease. Electron microscopy, small angle X-ray scattering, and ultracentrifugation data of human and *P. furiosus* MR reveal a dual functional complex consisting of a $(Mre11)_2$/$(Rad50)_2$ heterotetrameric DNA processing head and a double coiled-coil linker.

Introduction

DNA double-strand breaks (DSBs) are highly cytotoxic and mutagenic (Game, 1993; Zdzienicka, 1996; Petrini et al., 1997; Luo et al., 1999; Stewart et al., 1999). DSBs can arise during replication and as products of ionizing radiation and genotoxic chemicals, but are also endonucleolytically generated intermediates in meiosis, mating type switching, and V(D)J recombination (Ward, 1988; Sun et al., 1991a; Bierne et al., 1997; Gellert, 1997; Michel et al., 1997). DSBs are predominantly repaired by two pathways. Nonhomologous end joining directly rejoins DSBs, whereas homologous recombination utilizes a sister chromatid or homologous chromosome as a template for DNA resynthesis and rejoining (Roth and Wilson, 1988; Sun et al., 1991b; Kadyk and Hartwell, 1992; Phillips and Morgan, 1994; Leach, 1996).

The Mre11/Rad50 (MR) complex plays a key role in DSB repair. Homologs of Mre11 and Rad50 are found in all kingdoms of life (the *E. coli* MR homolog is denoted SbcCD) and are essential for genome integrity (Aravind et al., 1999). Eukaryotic MR can contain a third component, Nbs1 or yeast XRS2, that links the MR complex to damage-induced cell cycle checkpoints (Carney et al., 1998; Varon et al., 1998).

In vivo, the MR complex is primarily involved in homologous recombination by participating in the generation of the 3′ ssDNA tails and possibly by bridging DNA ends or sister chromatids (Dolganov et al., 1996; Bressan et al., 1999; Yamaguchi-Iwai et al., 1999). The MR complex is also required for meiotic DSB processing and is involved in telomere maintenance, DNA damage detection, yeast nonhomologous end joining, and checkpoint signaling (Haber, 1998). The underlying molecular mechanisms of the MR complex are unclear, but its multiple functions suggest both structural and DNA processing roles.

In vitro, Mre11 orthologs have three major activities, ssDNA endonuclease, dsDNA 3′→5′ exonuclease, and DNA hairpin opening, all of which require Mn^{2+} ions (Connelly et al., 1998; Furuse et al., 1998; Paull and Gellert, 1998; Trujillo et al., 1998; Usui et al., 1998; Hopfner et al., 2000a). dsDNA exonuclease and hairpin opening additionally require Rad50 and ATP. In vivo, Mre11 facilitates generation of 3′ tails for strand invasion in homologous recombination, likely by acting in concert with a 5′→3′ exonuclease (Tsubouchi and Ogawa, 2000). However, the molecular basis for these diverse nuclease activities of Mre11 and their control by the Rad50-ATPase is poorly understood.

Rad50 resembles the structural maintenance of chromosome (SMC) proteins, which are involved in chromosome cohesion and chromatin condensation (Connelly et al., 1998). Rad50 consists of bipartite N- and C-terminal ATPase segments at the ends of a 600–900 amino acid long heptad repeat insertion. The N- and C-terminal ATPase segments assemble into a single ABC type ATPase domain at the end of a predicted antiparallel coiled-coil (Melby et al., 1998; Hopfner et al., 2000b). In vivo, ATP is essential for Rad50 function, and disruption of the ATP binding Walker motifs in the Rad50-ATPase domain leads to a Rad50 null phenotype (Alani et al., 1990). In vitro, Rad50 evidently binds DNA in an ATP-dependent manner, and ATP binding to the Walker motifs engaged two Rad50 ABC domains and induced a conformational switch (Raymond and Kleckner, 1993; Hopfner et al., 2000b). The engaged ATP bound ABC domain dimer binds DNA more tightly, suggesting ATP controls DNA binding by conformational switching and an engagement/disengagement cycle of the Rad50 ABC domain dimer.

Thus, to better understand the ATP-dependent molecular mechanism of the MR complex in DSB repair, we determined crystal structures of *Pyrococcus furiosus* Mre11 and Rad50 catalytic domains and examined the

[4] Correspondence: jat@scripps.edu
[5] Present address: Gene Center and Institute of Biochemistry, University of Munich, 81377 Munich, Germany.

interaction architecture and stoichiometry by electron microscopy, ultracentrifugation, and small angle X-ray scattering of the human and *Pyrococcus furiosus* MR complexes. The structure of the *P. furiosus* Mre11 in complex with dAMP and Mn^{2+} reveals a molecular mechanism consistent with the in vitro 3′→5′ nuclease activity and indicates that Mre11's active site geometry prohibits endonucleolytic cleavage of dsDNA, but allows endonucleolytic cleavage of ssDNA and partially unwound dsDNA ends or hairpins. Mapping of eukaryotic mutations onto *P. furiosus* Mre11 structure indicates that Nbs1/Xrs2 binds to eukaryotic Mre11 remote from the Mre11 active site. We furthermore show that Mre11 binds to the Rad50 coiled-coil region adjacent to the ABC domain. The specific location of a hydrophobic surface patch on this coiled-coil region indicates adjacent Mre11 and DNA binding sites on Rad50 and suggests a mechanism for ATP-dependent control of the Mre11 exonuclease by Rad50, by unwinding and/or repositioning DNA ends into the Mre11 active site. The electron microscopy, small angle X-ray scattering, and ultracentrifugation data reveal a M_2R_2 heterotetrameric architecture of the MR complex, consisting of a single DNA binding/processing head at one end of a double coiled-coil linker, which suggests a dual function of the MR complex in DNA processing and sister chromatid interaction. The heterotetrameric M_2R_2 complex reveals surprising similarity to the structural and functional architecture of DNA mismatch repair enzymes and ABC transporters.

Results and Discussion

Crystal Structure of the *P. furiosus* Mre11 Nuclease

To help reveal the molecular basis for the diverse nucleolytic activities of Mre11, we determined the structure of *P. furiosus* Mre11 by multiple anomalous diffraction phasing to 2.6 Å (Table 1). This Mre11 structure (residues 1–342) lacks 82 C-terminal residues, which does not affect endonucleolytic activity (Figure 1A), but facilitated crystallization. The resulting high quality experimental electron density (Figure 1B) revealed the presence of two equivalent Mre11 molecules in the asymmetric unit that are related by a noncrystallographic 2-fold symmetry axis.

P. furiosus Mre11 comprises two domains that interact at the active site (Figure 1C). Domain I is composed of two parallel mixed β sheets (β15, β14, β1–β3 and β5, β6, β4, β7–β9, β11, β10, respectively) that are flanked by seven α helices (A–D, D', E, E'; Figure 1C). Domain I contains five conserved phosphodiesterase motifs, which form the nuclease active site (Bressan et al., 1998; Tsubouchi and Ogawa, 1998). The phosphodiesterase motifs are situated in loops connecting the core β strands with their flanking α helices and place the active site at the center of a shallow surface depression on Domain I (Figures 1C and 1D). Domain I resembles in fold and active site location the catalytic domain of calcineurin like Ser/Thr phosphatases and the DNA base excision repair enzyme apurinic endonuclease 1 (APE1). However, although Mre11 and APE1 are both DNA repair nucleases, they evidently possess different active site architectures and are mechanistically distinct (Figure 1C; see next section). For instance, Mre11 tightly coordinates two Mn^{2+} ions by seven conserved residues whereas APE1 binds a single Mg^{2+} ion primarily via a single conserved glutamic acid residue (Mol et al., 2000). In contrast, the structure of the phosphodiesterase motifs of Mre11 closely resembles the di-metal (Fe/Zn) binding motifs of Ser/Thr phosphatases. This resemblance suggests that the di-metal nuclease mechanism of Mre11 is similar to the di-metal protein phosphatase mechanism of Ser/Thr phosphatases (Griffith et al., 1995). However, differences in the active site geometry surrounding the immediate metal coordinating motifs reflect the distinct substrate specificities of the Ser/Thr protein phosphatases (phosphorylated proteins) and Mre11 (DNA).

Domain II, which consists of a 5-stranded β sheet (β12, β13, β16–β18) and two α helices, partially caps the active site phosphodiesterase motifs of Domain I, suggesting that Domain II plays a role in DNA substrate specificity (Figure 1C). This Domain II cap appears to be a unique Mre11 feature as no equivalent domain or fold is found in the protein phosphatases, APE1, or in a DALI search of the Protein Data Bank. Some rotational flexibility between Domains I and II (experimentally observed by comparing the two molecules in the asymmetric unit cell) may facilitate Mre11's binding to different DNA substrates including hairpins, ssDNA, and dsDNA ends. Despite this small rotational flexibility, the rms deviation in C_α atoms between both molecules in the asymmetric unit is only 0.7 Å. Since Domain II is attached to Domain I by three peptide linker chains and a 1850 $Å^2$ large aromatic interface, the overall orientation of Domain II with respect to Domain I appears rigid.

Mre11 Active Site and Nuclease Mechanism

In Mn^{2+}-containing crystals, we observed electron density for two Mn^{2+} ions, resembling the di-metal active site found in Ser/Thr protein phosphatases (Figure 2A). The two Mn^{2+} ions are octahedrally coordinated by seven conserved residues of the phosphodiesterase motifs (Asp8, His10, Asp49, Asn84, His173, His206, His208) and by a bridging water molecule. The four histidine nitrogen ligands are consistent with a preference of Mre11 for Mn^{2+} over Mg^{2+}, which is typically coordinated by all oxygen ligands (Glusker, 1991). In fact, in a crystal form containing Mg^{2+} instead of Mn^{2+}, we observe only electron density corresponding to one Mg^{2+} ion bound to the active site, which is not sufficient for catalysis, suggesting why Mre11 is inactive in the presence of Mg^{2+} (K.P.H., unpublished data).

To reveal the phosphodiesterase mechanism of Mre11, we soaked *P. furiosus* Mn^{2+}-Mre11 with *d*eoxy-*a*denosine *m*ono*p*hosphate (dAMP represents a product of an exonucleolytically cleaved DNA end) and determined the dAMP-Mn-Mre11 complex structure to 2.2 Å resolution (Figure 2A; Table 1). The Mre11 active site binds dAMP mainly via the phosphate moiety, which is liganded to Asn84 and His85 and to both Mn^{2+} ions. The double coordination of the dAMP phosphate by both active site metals resembles the binding of phosphorylated protein residues in Ser/Thr phosphatases, further supporting a common phosphoesterase mechanism be-

Table 1. Crystallographic Data Collection and Analysis

MAD Data Collection (SeMet-Mre11)				
Space group: $P2_12_12_1$ (2 molecules/asymmetric unit)				
Unit cell dimensions (Å): a = 73.1, b = 87.0, c = 146.3				
Data set	SeMet λ1	SeMet λ2	SeMet λ3	SeMet λ4
Wavelength (Å)	0.96112	0.97951	0.97969	0.99987
Data range (Å)	30.0–2.6	30.0–2.4	30.0–2.6	30.0–2.8
Observations (unique)	442,453 (29,437)	578,934 (39,228)	442,289 (29,321)	217,379 (23,713)
Completeness (%) (last shell)	82.4 (36.9)[a]	92.4 (66.8)[a]	94.0 (60.3)[a]	98.4 (98.8)
R_{sym}[b] (last shell)	0.055 (0.268)	0.044 (0.216)	0.049 (0.249)	0.048 (0.384)

Refinement	Mre11 + Mn^{2+} + dAMP	Rad50-ATPase
Space group	$P2_12_12_1$	$P3_121$
Unit cell dimensions (Å)	a = 74.3, b = 88.7, c = 145.1	a = b = 99.5, c = 116.4
Resolution range (Å)	20–2.2	20–3.0
Observations (unique)	431,781 (48,885)	119,376 (13,527)
Completeness (%) (last shell)	98.1 (86.1)	83.0 (47.3)
R_{sym}[a] (last shell)	0.046 (0.326)	0.057 (0.348)
Reflections F > 0 (cross validation)	47,867 (2,397)	11,886 (605)
Non-hydrogen atoms (solvent molecules)	5,806 (274)	3,002 (64)
R_{cryst}[c] (R_{free}[d])	0.222 (0.269)	0.256 (0.291)
Rms bond length (Å)/bond angles (°)	0.012/1.3	0.009/1.5
% core (disallowed) in Ramachandran plot	88 (0.0)	78 (0.0)

[a] Anomalous completeness.
[b] R_{sym} is the unweighted R value on I between symmetry mates.
[c] $R_{cryst} = \Sigma_{hkl}||F_{obs}(hkl)| - |F_{calc}(hkl)||/\Sigma_{hkl}|F_{obs}(hkl)|$.
[d] R_{free} = the cross validation R factor for 5% of reflections against which the model was not refined.

tween Mre11 and Ser/Thr phosphatases (Griffith et al., 1995).

The dAMP sugar moiety is situated in a groove formed by the Domain I–Domain II interface (Figure 2A). The sugar 3′O forms a hydrogen bond to the His208 backbone N, suggesting that the dAMP may represent the 3′ terminal nucleotide in exonuclease activity. The hydrogen bond to the Mre11 backbone, however, could also form to an internal 3′ oxygen in bent single stranded or hairpin DNA, in endonuclease or hairpin nicking activity (see below). The sugar binding groove extends from both sides of the bound dAMP and possesses several positively charged residues at the 3′ side of dAMP. The positively charged residues likely bind the adjacent, probably bent ssDNA backbone in endonuclease activity.

The adenine base of dAMP has no specific interactions with Mre11, as expected for a nonspecific endo/exonuclease. Mre11 binds dAMP primarily via the phosphate which exposes the Watson-Crick face of the adenine moiety, suggesting that Mre11 recognizes the terminal base intrahelically. Tyr187 likely stacks against the base of the terminal nucleotide in DNA exonuclease reactions (Figure 2A).

dAMP is bound to the active site of Mre11 in an orientation suggesting that Mre11 cleaves the sugar-3′-O-phosphate bond of DNA. The conserved phosphodiesterase residue His85, which is essential for the nuclease activity of Mre11 (Bressan et al., 1998), arguably acts in transition state stabilization (Figure 2A). His85 likely donates a proton to the leaving DNA 3′-OH (Figure 2B). The protonated state of His85 is probably stabilized through a charge relay system with the adjacent and conserved His52. In the enzyme-DNA complex, Mn^{2+} ion (1) likely binds the attacking hydroxide ion as proposed for protein phosphatases (Rusnack, 2000). Collinear nucleophilic attack of the phosphoester by this hydroxide would result in the crystallographically observed product with both Mn^{2+} ions coordinating the dAMP phosphate (Figure 2A).

The structure of the *P. furiosus* dAMP-Mre11 complex suggests that Mre11 cleaves DNA ends 3′→5′, liberating a nucleotide with the phosphate bound to the 5′ sugar oxygen. These 5′-phosphorylated nucleotides are biochemically observed as main products of the Mre11 dsDNA exonuclease activity, and no significant 5′→3′ activity has been biochemically observed for Mre11 (Trujillo et al., 1998; Connelly et al., 1998). Our structure therefore supports the biochemically observed 3′→5′ nuclease direction as the main dsDNA exonuclease activity of Mre11. These results indicate that the generation of 3′ tails in homologous recombination in vivo requires an additional 5′→3′ nuclease, such as EXO1 suggested by genetic data (Tsubouchi and Ogawa, 2000), or the nuclease direction of Mre11 is modulated in vivo by yet uncharacterized factors.

Mre11 Functional Motifs

To identify functional motifs of Mre11, we mapped eukaryotic Mre11 mutations that are connected with human disease and yeast DSB repair/meiosis defects onto the structure of P. *furiosus* Mre11 (Figure 3A). Interestingly, several mutations map outside the phosphodiesterase motifs and may disrupt important protein interactions with Rad50, Nbs1/Xrs2, and/or DNA. The N117S mutation in human Mre11 leads to an ataxia telangiectasia-like disorder (ATLD), with cellular features similar to ataxia telangiectasia and Nijmegen breakage syndrome, and the analogous yeast mutation N113S leads to sensitivity to ionizing radiation (Stewart et al., 1999). N117 of human Mre11 maps to a surface loop between the conserved secondary structure elements αB and β3, at a position where human and yeast Mre11 possess a 33

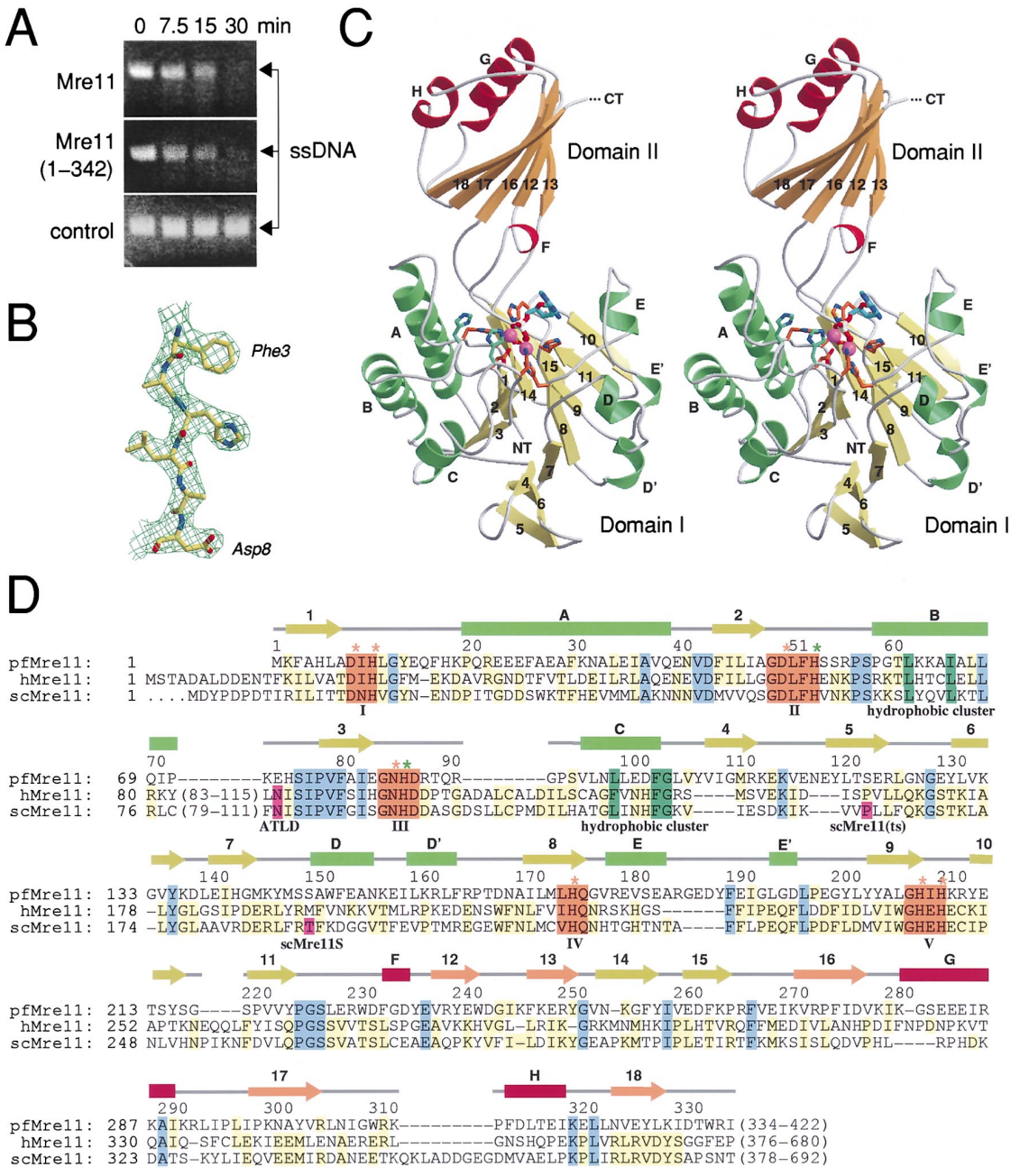

Figure 1. Structure and Activity of *P. furiosus* Mre11

(A) The crystallized *P. furiosus* Mre11(1–342) has wild-type Mre11-like ssDNA endonuclease activity. No activity is observed at low temperatures or in the absence of Mn^{2+} (control).

(B) Experimental MAD electron density (1σ) at the active site clearly defines carbonyl oxygen and side chain positions.

(C) Stereo view with annotated secondary structure shows the active site, bound dAMP, and the two domain fold of *P. furiosus* Mre11(1–342). Domain I (yellow strands, green helices) harbors the phosphodiesterase motifs (orange/green) that form the active site. Domain II (orange strands, red helices) completes the active site architecture by forming a likely DNA binding face adjacent to the phosphodiesterase motifs. dAMP (color-coded tubes) is bound via its phosphate moiety to two Mn^{2+} ions (magenta spheres) that are specifically coordinated by seven residues in the phosphodiesterase motifs (orange).

(D) Structure-guided sequence alignment of *P. furiosus* (pf) Mre11 with human (h) and yeast (sc) Mre11. The secondary structure of Figure 1C is shown above the alignment. Conserved residues are yellow (two out of three sequences) or blue (three out of three sequences). The phosphodiesterase motifs are orange. Residues involved in Mn^{2+} coordination and ester hydrolysis are labeled with orange and green stars, respectively. The location of human and yeast mutations (magenta) and of a conserved hydrophobic surface cluster likely involved in macromolecular interaction sites (green) are highlighted and annotated.

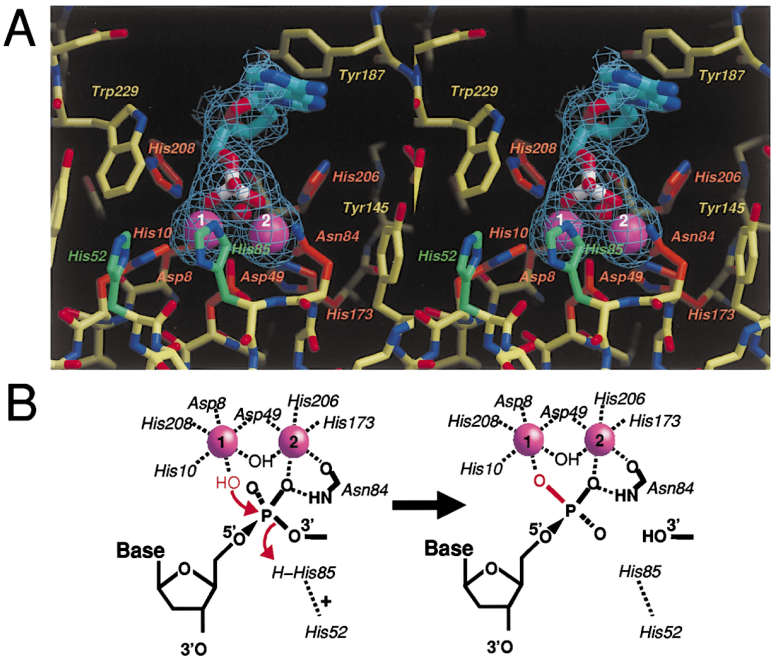

Figure 2. Mre11 Active Site and Implied Nuclease Mechanism

(A) *P. furiosus* Mre11 local active site geometry with simulated annealed Fo-Fc omit density (1.8σ) of the bound dAMP (blue and color-coded tubes) and Mn^{2+} ions (magenta spheres). The unbiased omit density shows the specific octahedral Mn^{2+} coordination by seven protein residues, a water molecule, and two phosphate oxygens. Only the phosphate and the sugar moieties of dAMP are specifically recognized by the protein, consistent with the nonsequence specific endo/exonuclease activities of Mre11.

(B) Proposed structure-based nuclease mechanism. Mn^{2+} ion (1) binds the attacking hydroxide ion (red). Collinear nucleophilic attack of this hydroxide leads to double Mn^{2+} ion coordination by the phosphate in the product state. His85/His52 are positioned to form a charge relay to protonate the leaving 3′O of the penultimate sugar.

residue insertion relative to *P. furiosus* Mre11 (Figure 1D). Since human Mre11-N117S interacts with Rad50 but fails to interact with Nbs1, this human and yeast insertion likely represents a unique eukaryotic binding site for Nbs1/Xrs2. Notably, this proposed Nbs1 binding insertion is located on Domain I opposite of the phosphodiesterase motifs, arguing that Nbs1 does not interact directly with the Mre11 active site. Experiments in which Nbs1 was found to stimulate Mre11's nuclease activity (Paull and Gellert, 1999) suggest that Nbs1 could act in trans within a proposed Mre11 homodimer (Johzuka and Ogawa, 1995; Furuse et al., 1998; Chamankhah et al., 2000; Paull and Gellert, 2000).

In yeast Mre11, P162S leads to temperature sensitivity of DSB repair (Mre11(ts)), and the Mre11 mutant fails to tightly interact with Rad50 and Xrs2 (Chamankhah et al., 2000). Yeast P162 maps to the β strand extension (β4–β6) of the core β sheet of Domain I, indicating that this region is involved in Mre11/Rad50/Xrs2 complex formation. Although the surface loops containing the ATLD and Mre11(ts) mutations are distant in sequence (Figure 1D), the mutation sites are only ~15 Å apart on the three-dimensional structure of *P. furiosus* Mre11 (Figure 3A). This adjacent mapped location suggests that both Nbs1 and Xrs2 bind to equivalent locations on human and yeast Mre11, respectively.

The yeast *mre11S* (separation of function) allele contains yeast P84S and T188I and leads to defective meiotic DSB processing, but normal mitotic DSB repair (Nairz and Klein, 1997). Yeast P84 is located in the proposed eukaryotic Nbs1/Xrs2 binding loop insertion and could disrupt the interaction of Mre11 with Xrs2 (Figure 1D). However, yeast T188 is located in a surface loop close to the active site (Figures 1D and 3A). This surface loop contains conserved positively charged residues and might participate in DNA binding by Mre11. T188I may therefore weaken or disrupt the interaction of Mre11 with DNA by distorting the surface next to the active site. Distortion of the yeast Mre11 DNA binding site would evidently affect processing of meiotic DSBs that require Mre11 nuclease activity.

Like the eukaryotic enzymes, *P. furiosus* Mre11 (MW 50 kDa) elutes from gel filtration chromatography with an apparent MW of a dimer (~120 kDa). A sequence conserved hydrophobic surface patch in αB and αC forms a symmetric Mre11 dimerization interface for the two molecules in the asymmetric unit and indicates a potential self-dimerization site of Mre11 (Figure 3B). The crystallized C-terminal truncated *P. furiosus* Mre11 (1–342), however, elutes with an apparent MW of a monomer (~60 kDa), suggesting the noncrystallographic dimer in the asymmetric unit probably forms during crystal packing. Therefore, the sequence conserved hydrophobic surface cluster and could equally be a Rad50 binding site. In any case, the conservation of a hydrophobic surface cluster in both archaeal and eukaryotic Mre11 plus the clustering of the hydrophobic, ATLD, and Mre11(ts) surface patches on Domain I identifies a likely macromolecular interaction site on Mre11 to form the Mre11/Rad50/Nbs1 complex (Figure 3A).

DNA Binding Mechanism and Nuclease Direction

The Mre11 structure reveals that the nuclease active site is situated in an L-shaped groove between Domains I and II that possesses the only significant positive surface potential for DNA binding (Figure 4A). To objectively and comprehensively evaluate all possible Mre11-DNA complexes, we used the complete systematic search program DOT to dock a dsDNA 12-mer to Mre11 (Roberts and Pique, 1999). In all 30 of the analyzed highest scoring solutions, DNA binds to the proposed L-shaped DNA binding groove (Figure 4A). The DNA binding orientation of the scissile strand in the docking solutions is consistent with the experimentally observed 5′→3′ binding orientation of dAMP, validating the computational approach. Furthermore, the docked DNA binds

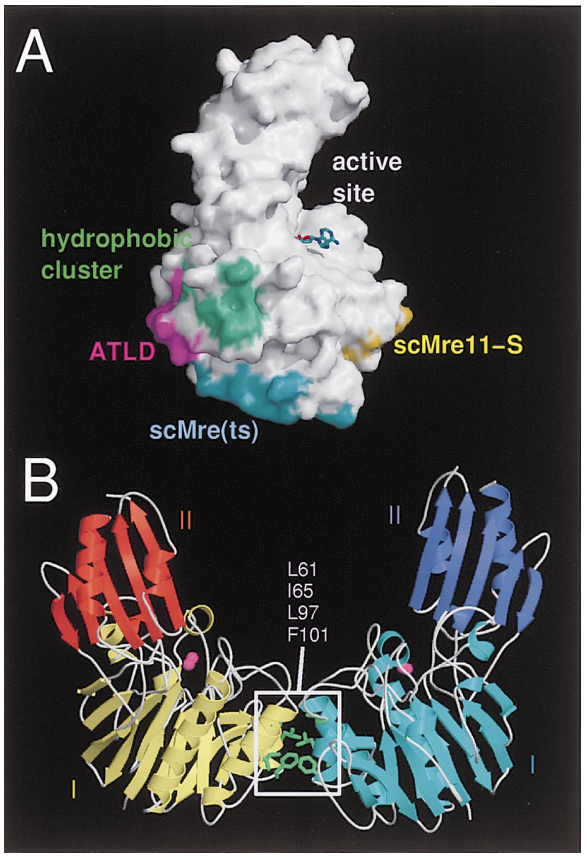

Figure 3. Mre11 Macromolecular Interaction Surface

(A) A surface cluster of mutations connected with human disease and yeast defects identifies an important surface area that is remote from the active site and evidently acts in macromolecular interactions of Mre11.

(B) The ribbon representation of the noncrystallographic Mre11 dimer (yellow/orange and cyan/blue with magenta manganese ions) identifies a conserved hydrophobic surface cluster (green side chains) which is a likely macromolecular interaction site in the MR complex formation.

similar in location and orientation as the DNA bound to the fold-related DNA repair enzyme APE1 (Mol et al., 2000). This similar DNA binding orientation suggests that APE1 and Mre11 recognize DNA in analogous ways, despite their evidently different nuclease mechanisms.

Although the dsDNA otherwise fits very well into the electropositive groove on both sides of dAMP, the shape of the active site depression at the Mn^{2+} ions requires a DNA backbone deformation by at least 5 Å from a B-DNA duplex across the DNA binding groove, in order to appropriately approach the catalytic metals for productive cleavage (Figure 4B). This 5 Å distance is not likely to be overcome by the observed rotational flexibility of Domain II with respect to Domain I; Domain II rotates along the DNA binding groove instead of across the DNA binding groove, suggesting rather a function in DNA translocation or conformational adaptability to accommodate different DNA end substrates. Since deformation or unwinding of a dsDNA duplex to approach the catalytic metals while bound to the DNA binding groove is energetically unfavorable, a dsDNA duplex might be sterically excluded from the active site metals, suggesting a mechanism for the inability of Mre11 to cleave dsDNA endonucleolytically. A mechanism in which a DNA duplex is bound by Mre11 but sterically excluded from cleavage is supported by biochemical experiments, showing that Mre11 can bind circular DNA and that Mn^{2+} ions are not required for DNA binding (Usui et al., 1998; de Jager et al., 2001). On the contrary, ssDNA, which possesses considerable conformational flexibility, could both bind to the electropositive groove and to the active site metals. Thus, ssDNA is likely not sterically excluded, suggesting a mechanism for Mre11's ssDNA endonuclease activity. Finally, DNA ends and hairpins could be partially unwound by Rad50 and ATP to approach the active site metals for nucleolytic attack, as indicated by biochemical data (Paull and Gellert, 1999). The structural and computational docking results therefore support a unified molecular mechanism for Mre11's broad but characteristic substrate specificity pattern by endonucleolytically cleaving both ssDNA and dsDNA ends/hairpins, the latter of which are partially unwound by ATP-Rad50 to expose ssDNA (Figure 4C).

Physical Link between Mre11 and the Rad50-ATPase Domain

In all organisms studied so far, Mre11 and Rad50 form a stable complex and are copurified together. To determine the Mre11 binding site on Rad50, we coexpressed and copurified *P. furiosus* Mre11 with *P. furiosus* Rad50-ATPase domain constructs that contained increasing lengths of the coiled-coil domain (Figures 5A and 5B). To ensure stable complex formation, copurification included a heat denaturation step plus three chromatography steps. We found that the ABC domain of Rad50 alone without the coiled-coil does not form a stable complex with Mre11, suggesting the coiled-coil contains the Mre11 binding site. In fact, the ABC domain plus the adjacent 40 amino acid long coiled-coil segment (denoted Rad50-ATPase) firmly bound Mre11 (Figures 5A and 5B). To estimate relative binding affinities of Mre11 to different Rad50 fragments, we dissociated immobilized Rad50/Mre11 complexes in a gradient of the denaturant guanidinium•HCl (see Experimental Procedures; data not shown). The full-length *P. furiosus* MR complex was stable up to 6.0 M guanidinium•HCl, whereas the truncated Mre11/Rad50-ATPase complex containing only a 40 residue long coiled-coil was stable up to 5.8 M guanidinium•HCl. This practically wild-type stability of the truncated Mre11/Rad50-ATPase complex suggests that the Mre11 binding site of Rad50 is located on an only 40 residue long coiled-coil region adjacent to the Rad50 ABC domain. This close linkage of the Rad50-ATPase to Mre11 provides a testable mechanistic basis for the requirement of Rad50-ATP hydrolysis for the Mre11 exonuclease activity.

Structure of the Mre11 Binding Rad50-ATPase Domain

To identify the structural nature and location of the Mre11 binding site on the Rad50 coiled-coil region, we crystallized and determined the structure of the Rad50-ATPase, containing the ATP binding cassette (ABC) domain and the biochemically identified 40 residue long Mre11 binding coiled-coil segment, to 3.0 Å resolution.

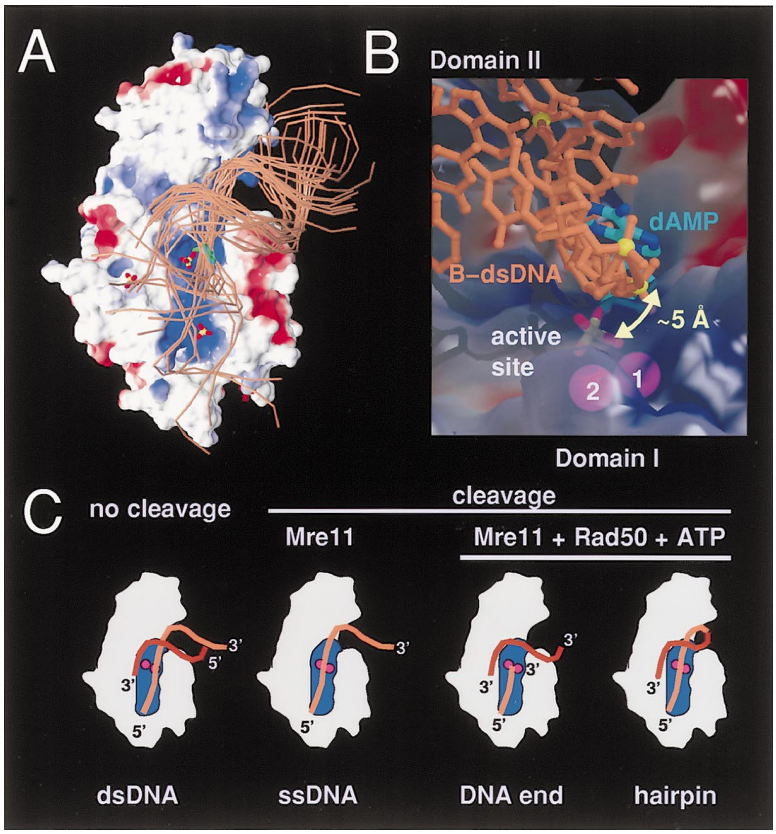

Figure 4. Active Site Channel and Proposed Mechanistic Basis for Multiple Nuclease Activities of Mre11

(A) Electrostatic surface calculated with UHBD (University of Houston Brownian Dynamics) and displayed from +2.5 kT/e$^-$ (blue) to −2.5 kT/e$^-$ (red). The electrostatic surface reveals a positive, L-shaped groove that extends in both directions from the active site at the corner of the L (shown by dAMP in green and color-coded tube representation), indicating the likely binding site for DNA. All of the top DOT docking solutions of a dsDNA 12-mer (brown tubes) are located in this L-shaped groove, overlap well with crystallographically bound sulfate ions (color-coded tubes), and are bound in the same 3′→5′ direction as dAMP.

(B) Structurally implied molecular mechanism for Mre11 substrate specificity. View along the active site DNA binding groove. dsDNA (brown tubes with yellow phosphates) fits well into the electropositive groove but has to be deformed ~5 Å from B-DNA to bind to the active site metals (magenta) due to the active site architecture. In contrast, ssDNA, dsDNA ends, or hairpins are destabilized or could be melted by ATP-Rad50 to reach the metals for ssDNA endonuclease and dsDNA exonuclease/hairpin nicking activity.

(C) Proposed unified mechanism for binding of different DNA substrates (ssDNA, DNA end, hairpin) and nonsubstrates (dsDNA) to the Mre11 DNA binding groove (blue). The scissile (light brown) and nonscissile (dark brown) DNA strands could be sufficiently deformed in ssDNA, DNA ends, or hairpins, but not in dsDNA, to approach the manganese ions (magenta) for cleavage.

The structure was solved by molecular replacement using the coordinates of the previously reported Rad50 ABC domain structure that lacked the Mre11 binding coiled-coil region (Hopfner et al., 2000b). The resulting electron density map revealed the new included antiparallel coiled-coil region that contains the Mre11 binding site of Rad50 (Figure 5C).

The structure of the Rad50-ATPase domain shows that the copurified and cocrystallized N- and C-terminal ATPase segments of Rad50 assemble into a single ABC domain attached to an antiparallel coiled-coil (Figure 5C). The ABC domain comprises two lobes (for details, see Hopfner et al., 2000b). Lobe I contains the ATP binding Walker A motif and is primarily formed by the N-terminal ATPase segment of Rad50. Lobe II contains the ATP-hydrolyzing Walker B and Signature motifs and is primarily formed by the C-terminal ATPase segment. Two major structural rearrangements in the ATPase domain of Rad50 occur upon ATP binding (Hopfner et al., 2000b). First, Lobe I rotates ~30° relative to Lobe II, most likely triggered by the His-Switch and Q-loop motifs (Figure 5C). Second, ATP binding engages two Rad50-ATPase domains into a compact homodimer.

The 40 residue long heptad repeat segments extend from the C and N termini of the two N- and C-terminal ABC ATPase segments, respectively, and assemble into an antiparallel coiled-coil (Figure 5C). This coiled-coil segment contains the Mre11 binding site based upon copurification and guanidinium•HCl dissociation (Figure 5B). Although the majority of this coiled-coil segment is hydrophilic in nature, it harbors a notable and conserved hydrophobic surface patch, which directly corresponds to the minimal Mre11 binding region (Figures 5D and 5E). This hydrophobic surface patch flanks a Lobe I surface area, which is the implicated DNA binding surface of Rad50, based on its electrostatic charge and on computational DNA docking analysis (Figure 5D; Hopfner et al., 2000b). These two flanking Mre11 and DNA binding sites on Rad50 suggest that Rad50 and Mre11 assemble to form a coupled DNA binding surface.

The coiled-coil region containing the Mre11 binding site is tightly anchored to Lobe II, contributing two of the four α helices that form Lobe II (Figure 5C). Thus, the ATP-induced rotation of Lobe I with respect to Lobe II would reposition the DNA bound to Lobe I with respect to the Mre11 bound to Lobe II. ATP-driven repositioning of DNA with respect to Mre11 is a specific and testable molecular mechanism for the ATP-driven nuclease activity of the MR complex. In particular, this mechanism is well suited to provide the energy for partially unwinding DNA ends or hairpins to allow appropriate substrate DNA to reach the active site Mn^{2+} ions of Mre11 for exonuclease cleavage (Figure 4C).

Architecture of the Mre11/Rad50 (MR) Complex

To elucidate the molecular architecture of the MR complex, we imaged human and *P. furiosus* MR by electron microscopy (EM). We observed particles consisting of

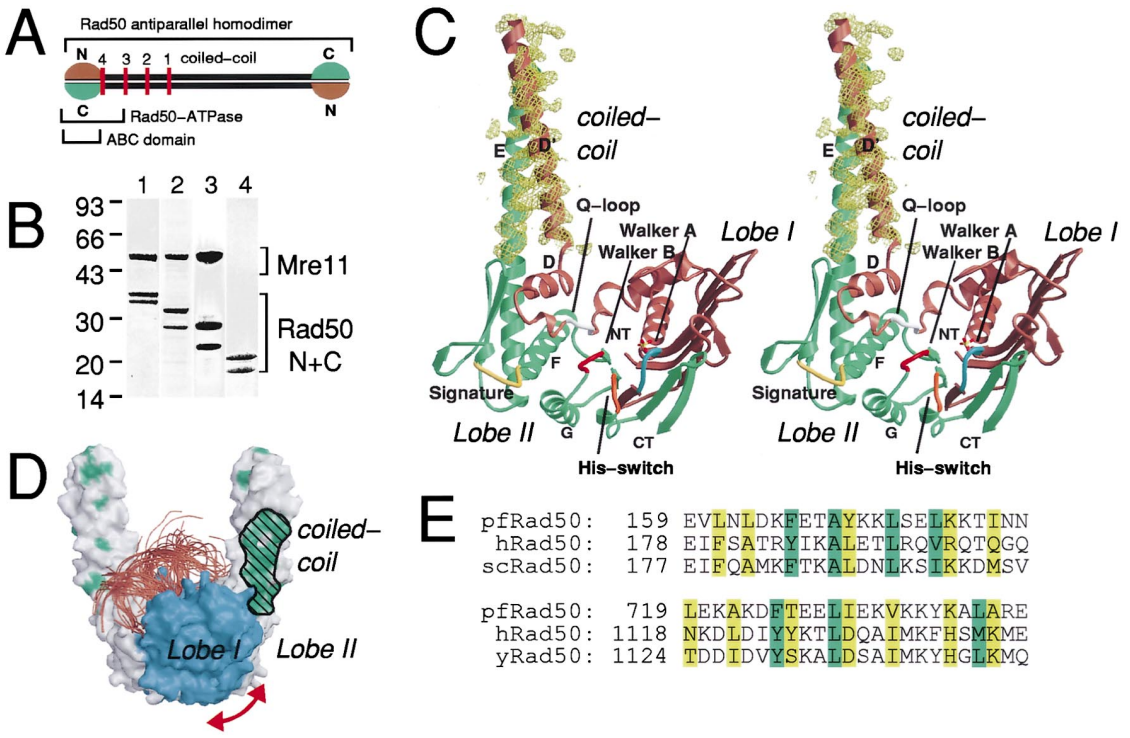

Figure 5. Structure of the Mre11 Binding Rad50-ATPase/Coiled-Coil Domain

(A) Schematic antiparallel dimer formation, consistent with previously published structural information, assembles N- and C-terminal Rad50-ATPase segments (green/brown) into two ABC domains at the ends of a coiled coil.

(B) Copurification of coexpressed Mre11 and Rad50 N- and C-terminal ATPase constructs. The bi-cistronic Rad50 constructs (lanes 1–4) contain decreasing lengths of the coiled-coil domain (indicated by red bars in Figure 5A). Surprisingly, only 40 amino acids of the coiled-coil (lane 3) are sufficient for stable complex formation of Mre11 with the Rad50-ATPase domain allowing the precise localization of the Mre11 binding region on Rad50.

(C) Stereo view of the crystallographically determined Rad50-ATPase domain structure that contains the Mre11 binding site (lane 3 in Figure 5B). The ribbon diagram with secondary structure shows the formation of the two lobed ABC ATPase fold by association of the N- (brown) and C-terminal (green) ATPase segments. The antiparallel coiled-coil was clearly visible in difference electron density (yellow contour at 1.8σ) after molecular replacement and is intimately attached to Lobe II. Catalytically important motifs that are mentioned in the text are highlighted and annotated.

(D) Macromolecular surface of the ATP bound engaged Rad50-ATPase domain dimer (Hopfner et al., 2000b) with the extended pair of helical coiled-coil structures and surface hydrophobicity (green). Each of the protruding helical coiled-coils possesses a hydrophobic surface patch (hatched, only one is visible in this view) that corresponds to the experimentally implicated Mre11 binding region as shown by copurification (Figure 5B, lane 3). ATP binding induces a rotation (double arrow) in Domain I (blue) that will reposition the implicated DNA binding surface (highest scoring DOT docking solutions cluster at the previously identified DNA binding surface) with respect to the newly defined Mre11 binding site. The adjacent location of implicated Mre11 and DNA binding sites on Rad50 imply a coupled Mre11-Rad50 DNA binding surface.

(E) Sequence alignment of the experimentally defined Mre11 binding coiled-coil segment shows conservation in the hydrophobic surface cluster (green). Residues forming the coiled-coil core are highlighted in yellow.

a large globular complex (head) at the end of a long coiled-coil structure (linker) (Figure 6A). Tetrameric head complexes were also observed in EM images with the purified *P. furiosus* Mre11/Rad50-ATPase complex that lacks most of the coiled-coil domain, suggesting the globular head complexes consists of Mre11 and the Rad50-ATPase domain (Figure 6A). In EM images containing dsDNA, several MR particles evidently bind DNA via the head complex (Figure 6B), further indicating that the head consists of Mre11 and the Rad50-ATPase domain, both of which bind to DNA.

The dimensions of the head ($\sim$50 Å radius) match the dimensions of a heterotetramer containing two Mre11 and two Rad50 molecules (M_2R_2). To confirm this heterotetrameric M_2R_2 architecture, we performed small angle X-ray scattering (SAXS) experiments on the *P. furiosus* Mre11/Rad50-ATPase complex (Table 2) and analytic equilibrium ultracentrifugation of the full-length *P. furiosus* MR complex (Figure 6C). SAXS measures the solution radius of gyration (R_{gyr}), whereas ultracentrifugation determines the molecular weight. The Mre11/Rad50-ATPase complex has a R_{gyr} of 51 Å in the absence of ATP and of 46 Å in the presence of ATP. The radii match the 50 Å radius of the head complexes in the EM images (Table 2). Since the Rad50 ABC domain in the absence of Mre11 is a monomer and dimerizes only in the presence of ATP (Hopfner et al., 2000b), the M_2R_2 heterotetramer is probably preformed by Mre11 self-dimerization. However, in the M_2R_2 heterotetramer, ATP consequently engages the two Rad50-ATPase domains more closely, indicated by the $\sim$10% decrease in R_{gyr} in the presence of ATP.

Analytic ultracentrifugation of the *P. furiosus* MR complex revealed a MW of 311 $\pm$ 40 kDa, consistent with an M_2R_2 heterotetramer (calculated MW 308 kDa; Figure

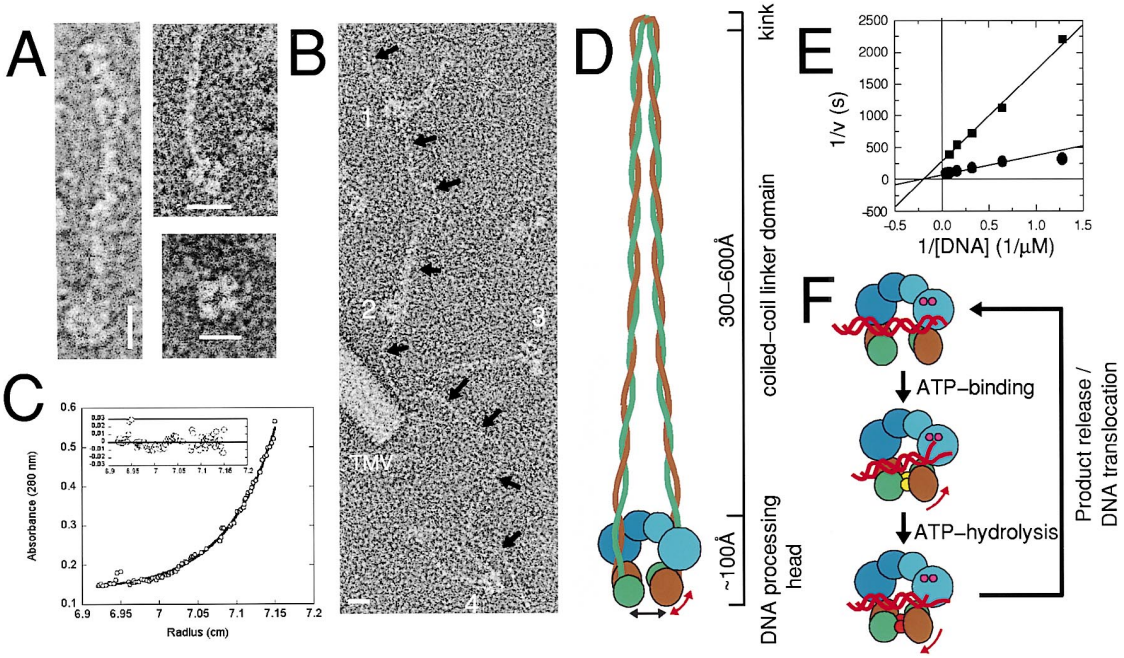

Figure 6. Architecture of the Mre11/Rad50 Complex

(A) Electron micrographs (EMs) of human MR (left) and *P. furiosus* MR (top right) show a globular head of 50 Å radius at the end of an extended coiled-coil structure (bar 100 Å). This head is also evident in EMs of *P. furiosus* Mre11/Rad50-ATPase (bottom right), and its size and tetrameric shape indicates formation of a stable heterotetramer of two Mre11 and two Rad50-ATPase domains at the end of a double coiled-coil.

(B) EMs in the presence of DNA indicate that the *P. furiosus* MR complex binds DNA (black arrows) with the globular head (particles 1 and 2). Comparison of MR particles that are presumably bound to DNA (1 and 2) with MR particles not bound to DNA (3 and 4) suggests that the tertiary structure of MR is not significantly altered by DNA binding, supporting a preformed M_2R_2 heterotetramer. TMV denotes a tabacco mosaic virus particle added for scaling (bar 100 Å).

(C) Sedimentation equilibrium of *P. furiosus* MR. The radial scan fits a single species model (residuals are shown in inset). The apparent molecular weight is 311 ± 40 kDa, indicating formation of a M_2R_2 heterotetramer (calculated MW 308 kDa).

(D) Model of the M_2R_2 heterotetramer based on EM, ultracentrifugation, SAXS, and crystal structure analysis. Rad50-ATPase Lobe I/II (brown/green) and the Mre11 dimer (light/dark blue) form a single DNA processing head at the end of a double coiled-coil linker (brown/green). ATP rotates Rad50-ATPase Lobe I with respect to Lobe II (red arrow) and promotes a Rad50-ATPase engagement/disengagement (black arrow).

(E) Double reciprocal plot of the exonuclease activity of the *P. furiosus* MR complex in the presence of ATP (circles) and AMP-PNP (squares), as monitored by the steady state fluorescence from the release of 2-aminopurine bases. These results show that ATP hydrolysis alters k_{cat}, but not K_m, for the end cleavage of a 27-mer duplex. The line fit represents nonlinear curve fitting to the Michaelis-Menten equation.

(F) Proposed molecular mechanism for the MR complex in DNA processing. After ATP-driven DNA binding to the M_2R_2 heterotetramer (see Figure 6D for color coding; ATP/ADP are shown as yellow/orange spheres, respectively), DNA double-strand breaks (red) are bound and possibly partially unwound to enable cleavage by Mre11. ATP hydrolysis by Rad50 induces a conformational change (red arrows) that likely promotes product release or translocation. For clarity, the coiled-coil and symmetric second DNA binding site (in the back) are not shown.

6C). Together, these EM, SAXS, and ultracentrifugation data reveal that in the full MR complex, two Mre11 bind to two Rad50-ATPase domains, forming a single hetero-tetrameric DNA processing head at the end of the coiled-coil domains (Figure 6D).

The EM images indicate that the coiled-coil linker lengths of 600 Å (human) or 300 Å (*P. furiosus*) and widths of 40 Å (human and *P. furiosus*) of the M_2R_2 complex are exactly half the length but twice the width of a fully extended coiled-coil. The EM results thus indicate that the Rad50 coiled-coil typically kinks back in the middle and might form a loose four helix bundle composed of two coiled-coils (Figure 6D). Although the structure of the kink is currently unknown, the evident

Table 2. Small Angle X-Ray Scattering of *P. furious* Mre11 and Rad50-ATPase

	R_{gyr} (R^{cryst}_{gyr})	MW ($MW^{calc}_{monomer}$)	Composition
Mre11	40.7 ± 0.9 (n.d.)	118 (50)	dimer
Rad50-ATPase (+ ATP)	35.1 ± 1.5 (34.9)	80 (43)	dimer
Mre11/Rad50-ATPase	50.9 ± 3.5 (n.d.)	231 (50 + 43)	heterotetramer
Mre11/Rad50-ATPase (+ ATP)	46.3 ± 3.8 (n.d.)	174 (50 + 43)	heterotetramer

R_{gyr}: Radius of gyration (Å). Average of typical four dilutions ± standard deviation.
R^{cryst}_{gyr}: Radius of gyration calculated from X-ray structure.
MW: R_{gyr} estimated molecular weight in kDa.
$MW^{calc}_{monomer}$: sequence estimated molecular weight of monomer in kDa.

similarity of this Rad50 coiled-coil structure with the structure of SMC proteins (that are involved in chromatid interaction) suggests that the M_2R_2 coiled-coil linker could play a role in sister chromatid interactions or in the interaction of two broken DNA ends (Melby et al., 1998; Bressan et al., 1999).

Structural and Functional Model for the Mre11/Rad50 DNA Processing Complex

Taken together, our data suggest a dual role for the MR complex in DSB repair. The $(Mre11)_2$/$(Rad50\text{-}ATPase)_2$ head likely functions in ATP-dependent DNA processing in meiosis and mitotic DSB repair, while the extended coiled-coil domain could serve as linker in sister chromatid interaction (Bressan et al., 1999). Mechanistically, the conformational changes of the Rad50-ATPase domain upon ATP binding are well suited to prepare DNA ends/hairpins for nucleolytic cleavage by Mre11. This model is supported by results from a steady-state exonuclease assay that measures the release of the fluorescent adenine analog 2-aminopurine from dsDNA (Figure 6E). In the presence of the nonhydrolyzable ATP analogs AMP-PNP or ATPγS, the exonuclease activity of the *P. furiosus* MR complex is only $\sim$3–5 times slower than in the presence of ATP, while no activity was found in the presence of ADP, consistent with data from the *E. coli* homologs (Connelly et al., 1997). The k_{cat} and K_m values for dsDNA cleavage by the MR complex in the presence of ATP (K_m = 4.7 μM ($\pm$ 0.7); k_{cat} 0.0062 s^{-1} ($\pm$ 0.0004)) or AMP-PNP (K_m = 5.0 μM ($\pm$ 0.6) and k_{cat} 0.0016 s^{-1} ($\pm$ 0.0008)) suggest that ATP hydrolysis mostly accelerates k_{cat} without altering K_m. The similar K_m values suggest that both the ATP and AMP-PNP bound forms of Rad50 bind DNA with similar affinities, in agreement with the structural data, where ATP and AMP-PNP have equivalent conformational effects on the Rad50-ATPase domain (Hopfner et al., 2000b). As ATP hydrolysis merely accelerates the k_{cat} of the Mre11 exonuclease, but is not required for initial exonucleolytic cleavage per se, ATP hydrolysis appears to accelerate product release after the Mre11 cleavage reaction. Taken together, our results support the following working model for DNA processing by the MR complex (Figure 6F): ATP binding to Rad50 prepares DNA substrates for cleavage by Mre11, likely via engagement of two Rad50-ATPase domains plus rotation of Lobe I with respect to Lobe II (Figure 5D). After nucleolytic cleavage of the prepared ends by Mre11, ATP hydrolysis accelerates product release for subsequent cleavage reaction. A likely mechanism for enhancing release of product would be disengagement of the ATPase domain dimer to disrupt the interaction of the MR complex with DNA (Hopfner et al., 2000b). Notably, the M_2R_2 heterotetramer has the ability to simultaneously process two DNA ends, which might be important in the initial search for microhomologies and/or annealing of two broken ends.

Implications for ABC-ATPase Machines in DNA Repair and Membrane Transport

The heterotetrameric M_2R_2 DNA processing head is surprisingly similar in its overall architecture to other ABC ATPase machines, such as the ABC transporter and MutS family DNA mismatch repair enzymes. These multidomain enzymes all contain an ABC-ATPase dimer plus a substrate/function-specific dimer as revealed here for the M_2R_2 heterotetramer (Fishel and Wilson, 1997; Kolodner and Marsischky, 1999; Holland and Blight, 1999). The crystal structures of the ATP bound Rad50 ABC domain (Hopfner et al., 2000b) and ADP bound or nucleotide free MutS (Lamers et al., 2000; Obmolova et al., 2000) revealed that the ABC dimer orientation in both complexes is surprisingly similar. In fact, the location of the MutS domains connecting the MutS ABC and DNA binding domains corresponds directly to the identified coiled-coil segment linking the Rad50 ABC domain to Mre11. Likewise, the most frequent cystic fibrosis causing mutation in the cystic fibrosis transmembrane transporter (ΔF508), which results in subunit detachment between the transmembrane channel domains and the ABC domains, maps essentially to the Mre11 binding coiled-coil surface patch on Rad50 (Hung et al., 1998; Hopfner et al., 2000b). Therefore, our results suggest that the substrate-specific domains in ABC transporter, MutS mismatch repair enzymes, and Mre11/Rad50 are attached to the respective ABC dimer in a similar location. This striking architectural similarity suggests that the ABC dimer controls the corresponding substrate-specific domains in ABC transporter and DNA mismatch repair enzymes in a similar way as we proposed for Mre11/Rad50.

Experimental Procedures

Protein Expression and Purification

All *P. furiosus* proteins were synthesized in *E. coli* BL21-RIL (DE3) (Stratagene) and purified and characterized as described (Hopfner et al., 2000a, 2000b). Selenomethionine-Mre11 was synthesized in *E. coli* B834 (Novagen) in minimal medium supplemented with selenomethionine. The human MR complex was produced from recombinant baculovirus expression in insect cells and purified by Ni^{2+} affinity and gel filtration chromatography.

Crystallization, Crystallographic Data Collection, MAD Phasing, and Structure Refinement of *P. furiosus* Mre11

P. furiosus Mre11(1–342) (12 mg/ml in 20 mM phosphate [pH 7.5], 200 mM NaCl, 0.1 mM EDTA, 5% glycerol) was crystallized in space group $P2_12_12_1$ with cell dimensions a = 72.9, b = 87.0, c = 146.4 Å and two molecules in the asymmetric unit by sitting drop vapor diffusion at 4°C after mixing 2 μl protein solution with 1.5 μl precipitant solution (100 mM Ches [pH 9.5], 400 mM ammonium sulfate, 35% PEG 600). Four wavelength multiple anomalous diffraction (MAD) data to 2.6 Å were recorded at 100 K with a Quantum 2$\times$2 CCD detector at BL 5.0.2 (Advanced Light Source) and processed with the HKL suite (Otwinowski, 1993) (Table 1).

Six selenium sites were located with SOLVE (Terwilliger and Berendzen, 1999) and used to calculate initial phases with MLPHARE (CCP4, 1994). The remaining four selenium sites were located in difference Fourier maps calculated from the initial phases. Phases to 2.8 Å were calculated with MLPHARE and improved with SOLOMON (CCP4, 1994). The resulting high quality electron density (Figure 1B) was used to trace both molecules in the asymmetric unit with MAIN (Turk, 1992). After overall anisotropic B-value and bulk solvent correction, the structure was refined to 2.6 Å by cycles of positional and individual B-value refinement and manual model building with CNS (Brünger et al., 1998) and MAIN (Table 1). Five percent of the data were excluded from refinement to calculate the free R value for cross validation. Initial NCS restraints were gradually removed in later stages of refinement. Mn^{2+} + dAMP containing *P. furiosus* Mre11 was prepared by incubation of the crystal in mother liquor containing 1 mM $MnCl_2$ and 10 mM dAMP for 3–5 hr at 4°C. Data to 2.1 Å were collected at BL9-2 at SSRL using a Quantum 2$\times$2

CCD detector. The models were rebuilt with MAIN and refined with CNS. Refinement and model statistics are shown in Table 1.

Crystallization, Crystallographic Data Collection, Phasing, and Structure Refinement of the *P. furiosus* Rad50-ATPase Domain

The Rad50-ATPase domain was crystallized in space group $P3_121$ by mixing 2 μl of protein solution (8 mg/ml in 20 mM phosphate, [pH 7.5], 200 mM NaCl, 0.1 mM EDTA, 5% glycerol) with 2 μl precipitant (100 mM Na-Acetate [pH 6.2], 8% Peg 6K, 10 mM Ca-Acetate) using sitting drop vapor diffusion. Data to 3.0 Å resolution were recorded at 100 K with a Quantum 2×2 CCD detector at BL 5.0.2 (Advanced Light Source) and processed with the HKL suite (Table 1). Initial phases were calculated from a single AMoRe (Navaza, 1994) molecular replacement solution by using the previously published Rad50 ABC domain structure (lacking the coiled-coil) as search model. The additional coiled-coil domain was clearly apparent in 2Fo-Fc and Fo-Fc density maps (Figure 5C) and traced with MAIN. After overall anisotropic B-value and bulk solvent correction, the structure was refined by cycles of positional and restrained individual B-value refinement and by manual model building with CNS and MAIN (Table 1).

Nuclease Assays

Endonuclease assays on single-stranded ϕX174 DNA were performed as described (Hopfner et al., 2000a). Steady state 2-AP fluorescence assays were performed in a SLM8100 spectrofluorimeter essentially as described (Lam et al., 1999), by using 310 nm excitation and 375 emission settings. Assays were performed at 50°C in 50 mM Tris, (pH 7.8), 150 mM NaCl, 0.1% Peg 6K, 2.5% glycerol, 1 mM $MnCl_2$, 5 mM $MgCl_2$ using 1 mM of the indicated nucleotide, 0.2 μM protein, and 1–12.5 μM dsDNA oligonucleotide (5′-GGCG TGCCTTGGGCGCGCTGCGGGCGG(2-AP)G; six 2-fold dilutions). Linear rates were followed for 30–300 s and analyzed with SigmaPlot (Jandel). To rule out contaminating *E. coli* exonuclease activity, we did a temperature profile of the exonuclease reaction. The activity dramatically increases at high temperatures for both ATP and ATPγS bound *P. furiosus* MR, with the optimum beyond 65°C. This activity profile is a signature of hyperthermophilic proteins such as Mre11 and Rad50 from *P. furiosus* and rules out contaminating activity. No significant activity was found at 37°C where an *E. coli* contamination would have its optimum activity.

Dissociation of Mre11 and Rad50 in Guanidinium•HCl

Copurified P. *furiosus* 6×His-Mre11/Rad50 and Mre11/Rad50-ATPase-6xHis was bound to 1 ml Ni-NTA sepharose column (Qiagen) and eluted in 20 mM phosphate (pH 8.0), in gradient from 0 to 6 M guanidium•HCl (in 120 mM NaCl, 5% glycerol, 4 mM imidazol). Eluted subunits were detected with SDS-PAGE.

Electron Microscopy

Carbon-coated copper grids were glow-discharged for 1 min in the presence of amyl amine and floated on top of 5 μl drops containing 20–50 μg/ml protein for 2 min. The grids were stained in 3% uranyl acetate and viewed on a Philips CM120 microscope at 100 kV in low dose mode.

Small Angle X-Ray Scattering

Data were recorded at SSRL beamline 4–2 typically using four protein concentrations (1, 2, 4, 8 mg/ml) in 20 mM Tris (pH 7.5), 200 mM NaCl, 5% glycerol, 5 mM $MgCl_2$, ± 0.5 mM ATP). R_{gyr} was derived from experimental data with GNOM (Svergun, 1993).

Analytical Ultracentrifugation

Equilibrium sedimentation was done in a Beckman XL-1 ultracentrifuge with a An60Ti rotor. Sedimentation equilibrium was recorded after 20 hr at 7000 rpm at 20°C, using 0.4 mg/ml protein (in 20 mM Tris, [pH 7.2], 150 mM NaCl, 1 mM EDTA). Data were analyzed by Origin (Microcal).

Figure Preparation

Structure figures were made with MOLSCRIPT (Avatar Software AB) and Raster3D (Merritt and Bacon, 1997). Figures 3A and 5D were prepared using GRASP (Nicholls et al., 1991). Figure 4A was made with AVS and UHBD.

Acknowledgments

We thank S. Parikh for help with data collection, the staff of beamlines 5.0.2 (ALS) and 9–2 (SSRL) for assistance, H. Tsuruta (beamline 4-1, SSRL) and C. Putnam for help with SAXS data collection and processing, D. Millar and M. Bailey for help with fluorescence assays, J.-L. Pellequer for help with computational docking simulations, and J. Kelly and S. Deechongkit for help with analytic ultracentrifugation. We thank C. Putnam, D. Shin, and C. Mol for comments on the manuscript. This work was supported by DOE (DE-AC03-76SF00098) and NSF (DBI 9904559) and by a research project grant (CCE-99424) from the American Cancer Society (to J.P.C.). L.C. is supported by a grant from the Canadian Institutes of Health research, and K.P.H. by The Skaggs Institute for Chemical Biology and a BASF Fellowship from the Studienstiftung des deutschen Volkes e.V.

Received February 27, 2001; revised April 13, 2001.

References

Alani, E., Padmore, R., and Kleckner, N. (1990). Analysis of wild-type and *rad50* mutants of yeast suggests an intimate relationship between meiotic chromosome synapsis and recombination. Cell *61*, 419–436.

Aravind, L., Walker, D.R., and Koonin, E.V. (1999). Conserved domains in DNA repair proteins and evolution of repair systems. Nucleic Acids Res. *27*, 1223–1242.

Bierne, H., Ehrlich, S.D., and Michel, B. (1997). Deletions at stalled replication forks occur by two different pathways. EMBO J. *16*, 3332–3340.

Bressan, D.A., Olivares, H.A., Nelms, B.E., and Petrini, J.H. (1998). Alteration of N-terminal phosphoesterase signature motifs inactivates Saccharomyces cerevisiae Mre11. Genetics *150*, 591–600.

Bressan, D.A., Baxter, B.K., and Petrini, J.H. (1999). The Mre11-Rad50-Xrs2 protein complex facilitates homologous recombination-based double-strand break repair in *Saccharomyces cerevisiae*. Mol. Cell. Biol. *19*, 7681–7687.

Brünger, A.T., Adams, P.D., Clore, G.M., DeLano, W.L., Gros, P., Grosse-Kunstleve, R.W., Jiang, J.S., Kuszewski, J., Nilges, M., Pannu, N.S., et al. (1998). Crystallography & NMR system: A new software suite for macromolecular structure determination. Acta Crystallogr. D *54*, 905–921.

Carney, J.P., Maser, R.S., Olivares, H., Davis, E.M., Le Beau, M., Yates, J.R., 3rd, Hays, L., Morgan, W.F., and Petrini, J.H. (1998). The hMre11/hRad50 protein complex and Nijmegen breakage syndrome: linkage of double-strand break repair to the cellular DNA damage response. Cell *93*, 477–486.

Chamankhah, M., Fontanie, T., and Xiao, W. (2000). The Saccharomyces cerevisiae mre11(ts) allele confers a separation of DNA repair and telomere maintenance functions. Genetics *155*, 569–576.

CCP4 (1994). The CCP4 suite: programs for protein crystallography. Acta Crystallogr. D *50*, 760–763.

Connelly, J.C., de Leau, E.S., Okely, E.A., and Leach, D.R. (1997). Overexpression, purification, and characterization of the SbcCD protein from *Escherichia coli*. J. Biol. Chem. *272*, 19819–19826.

Connelly, J.C., Kirkham, L.A., and Leach, D.R. (1998). The SbcCD nuclease of *Escherichia coli* is a structural maintenance of chromosomes (SMC) family protein that cleaves hairpin DNA. Proc. Natl. Acad. Sci. USA *95*, 7969–7974.

de Jager, M., Dronkert, M.L., Modesti, M., Beerens, C.E., Kanaar, R., and van Gent, D.C. (2001). DNA-binding and strand-annealing activities of human Mre11: implications for its roles in DNA double-strand break repair pathways. Nucleic Acids Res. *15*, 1317–1325.

Dolganov, G.M., Maser, R.S., Novikov, A., Tosto, L., Chong, S., Bressan, D.A., and Petrini, J.H.J. (1996). Human Rad50 is physically associated with hMre11: identification of a conserved multiprotein

complex implicated in recombinational DNA repair. Mol. Cell. Biol. *16*, 4832–4841.

Fishel, R., and Wilson, T. (1997). MutS homologs in mammalian cells. Curr. Opin. Genet. Dev. *7*, 105–113.

Furuse, M., Nagase, Y., Tsubouchi, H., Murakami-Murofushi, K., Shibata, T., and Ohta, K. (1998). Distinct roles of two separable in vitro activities of yeast Mre11 in mitotic and meiotic recombination. EMBO J. *17*, 6412–6425.

Game, J.C. (1993). DNA double strand breaks and the *RAD50-RAD57* genes in *Saccharomyces*. Cancer Biol. *4*, 73–83.

Gellert, M. (1997). Recent advances in understanding V(D)J recombination. Adv. Immunol. *64*, 39–64.

Glusker, J.P. (1991). Structural aspects of metal liganding to functional groups in proteins. Adv. Prot. Chem. *42*, 1–76.

Griffith, J.P., Kim, J.L., Kim, E.E., Sintchak, M.D., Thomson, J.A., Fitzgibbon, M.J., Fleming, M.A., Caron, P.R., Hsiao, K., and Navia, M.A. (1995). X-ray structure of calcineurin inhibited by the immunophilin-immunosuppressant FKBP12–FK506 complex. Cell *82*, 507–522.

Haber, J.E. (1998). The many interfaces of Mre11. Cell *95*, 583–586.

Holland, I.B., and Blight, M.A. (1999). ABC-ATPases, adaptable energy generators fueling transmembrane movement of a variety of molecules in organisms from bacteria to humans. J. Mol. Biol. *293*, 381–399.

Hopfner, K.P., Karcher, A., Shin, D., Fairley, C., Tainer, J.A., and Carney, J.P. (2000a). Mre11 and Rad50 from Pyrococcus furiosus: cloning and biochemical characterization reveal an evolutionarily conserved multiprotein machine. J. Bacteriol. *182*, 6036–6041.

Hopfner, K.P., Karcher, A., Shin, D.S., Craig, L., Arthur, L.M., Carney, J.P., and Tainer, J.A. (2000b). Structural biology of Rad50-ATPase: ATP-driven conformational control in DNA double-strand break repair and the ABC-ATPase superfamily. Cell *101*, 789–800.

Hung, L.W., Wang, I.X., Nikaido, K., Liu, P.Q., Ames, G.F.-L., and Kim, S.H. (1998). Crystal structure of the ATP-binding subunit of an ABC transporter. Nature *396*, 703–707.

Johzuka, K., and Ogawa, H. (1995). Interaction of Mre11 and Rad50: two proteins required for DNA repair and meiosis-specific double-strand break formation in Saccharomyces cerevisiae. Genetics *139*, 1521–1532.

Kadyk, L.C., and Hartwell, L.H. (1992). Sister chromatids are preferred over homologs as substrates for recombinational repair in *Saccharomyces cerevisiae*. Genetics *132*, 387–402.

Kolodner, R.D., and Marsischky, G.T. (1999). Eukaryotic DNA mismatch repair. Curr. Opin. Genet. Dev. *9*, 89–96.

Lam, W.C., Van der Schans, E.J., Sowers, L.C., and Millar, D.P. (1999). Interaction of DNA polymerase I (Klenow fragment) with DNA substrates containing extrahelical bases: implications for proofreading of frameshift errors during DNA synthesis. Biochemistry *38*, 2661–2668.

Lamers, M.H., Perrakis, A., Enzlin, J.H., Winterwerp, H.H., de Wind, N., and Sixma, T.K. (2000). The crystal structure of DNA mismatch repair protein MutS binding to a G x T mismatch. Nature *407*, 711–717.

Leach, D.R.F. (1996). Genetic Recombination (Oxford: Blackwell Science).

Luo, G., Yao, M.S., Bender, C.F., Mills, M., Bladl, A.R., Bradley, A., and Petrini, J.H. (1999). Disruption of mRad50 causes embryonic stem cell lethality, abnormal embryonic development, and sensitivity to ionizing radiation. Proc. Natl. Acad. Sci. USA *96*, 7376–7381.

Melby, T.E., Ciampaglio, C.N., Briscoe, G., and Erickson, H.P. (1998). The symmetrical structure of structural maintenance of chromosomes (SMC) and MukB proteins: long, antiparallel coiled coils, folded at a flexible hinge. J. Cell. Biol. *142*, 1595–1604.

Merritt, E.A., and Bacon, D.J. (1997). Raster3D: Photorealistic molecular graphics. Methods Enzymol. *277*, 505–524.

Michel, B., Ehrlich, S.D., and Uzest, M. (1997). DNA double-strand breaks caused by replication arrest. EMBO J. *16*, 430–438.

Mol, C.D., Izumi, T., and Mitra, S. and Tainer, J.A. (2000). DNA-bound structures and mutants reveal abasic DNA binding by APE1 and DNA repair coordination. Nature *403*, 451–456.

Nairz, K., and Klein, F. (1997). Mre11S-a yeast mutation that blocks double-strand-break processing and permits nonhomologous synapsis in meiosis. Genes Dev. *11*, 2272–2290.

Navaza, J. (1994). AMoRe: an automated package for molecular replacement. Acta Cryst. A *50*, 157–163.

Nicholls, A., Sharp, K., and Honig, B. (1991). Protein folding and association: insights from the interfacial and thermodynamic properties of hydrocarbons. Proteins *11*, 281–296.

Obmolova, G., Ban, C., Hsieh, P., and Yang, W. (2000). Crystal structures of mismatch repair protein MutS and its complex with a substrate DNA. Nature *407*, 703–710.

Otwinowski, Z. (1993). Data Collection and Processing, L. Sawyer, N. Isaacs, and S. Bailey, eds. (Warrington, UK: Science and Engineering Research Council).

Paull, T.T., and Gellert, M. (1998). The 3′ to 5′ exonuclease activity of Mre 11 facilitates repair of DNA double-strand breaks. Mol. Cell. *1*, 969–979.

Paull, T.T., and Gellert, M. (1999). Nbs1 potentiates ATP-driven DNA unwinding and endonuclease cleavage by the Mre11/Rad50 complex. Genes Dev. *13*, 1276–1288.

Paull, T.T., and Gellert, M. (2000). A mechanistic basis for Mre11-directed DNA joining at microhomologies. Proc. Natl. Acad. Sci. USA *97*, 6409–6414.

Petrini, J.H., Bressan, D.A., and Yao, M.S. (1997). The RAD52 epistasis group in mammalian double strand break repair. Semin. Immunol. *9*, 181–188.

Phillips, J.W., and Morgan, W.F. (1994). Illegitimate recombination induced by DNA double-strand breaks in a mammalian chromosome. Mol. Cell. Biol. *14*, 5794–5803.

Raymond, W.E., and Kleckner, N. (1993). RAD50 protein of *S. cerevisiae* exhibits ATP-dependent DNA binding. Nucleic Acids Res. *21*, 3851–3856.

Roberts, V.A., and Pique, M.E. (1999). Definition of the interaction domain for cytochrome c on cytochrome c oxidase: III. Prediction of the docked complex by a complete, systematic search. J. Biol. Chem. *274*, 38051–38060.

Roth, D.B., and Wilson, J.H. (1988). Illegitimate recombination in mammalian cells. In Genetic Recombination, R. Kucherlapati and G.R. Smith, eds. (Washington, D.C.: American Society for Microbiology), pp. 621–654.

Rusnack, F. (2000). Manganese activated Phosphatases. In Metal Ions in Biological Systems, A. Sigel and H. Sigel, eds. (Basel, Switzerland: Marcel Dekker).

Stewart, G.S., Maser, R.S., Stankovic, T., Bressan, D.A., Kaplan, M.I., Jaspers, N.G.J., Raams, A., Byrd, P.J., Petrini, J.H.J., and Taylor, A.M.R. (1999). The DNA double-strand break repair gene *hMRE11* is mutated in individuals with an ataxia-telangiectasia-like disorder. Cell *99*, 577–587.

Sun, H., Treco, D., Schultes, N.P., and Szostak, J.W. (1991a). Double-strand breaks at an initiation site for meiotic gene conversion. Nature *338*, 87–90.

Sun, H., Treco, D., and Szostak, J.W. (1991b). Extensive 3′-overhanging, single-stranded DNA associated with the meiosis-specific double-strand breaks at the ARG4 recombination initiation site. Cell *64*, 1155–1161.

Svergun, D.I. (1993). A direct indirect method of small-angle scattering data treatment. J. Appl. Cryst. *26*, 258–267.

Terwilliger, T.C., and Berendzen, J. (1999). Automated MAD and MIR structure solution. Acta Crystallogr. D. *55*, 849–861.

Trujillo, K.M., Yuan, S.S., Lee, E.Y., and Sung, P. (1998). Nuclease activities in a complex of human recombination and DNA repair factors Rad50, Mre11, and p95. J. Biol. Chem. *273*, 21447–21450.

Turk, D. (1992). Weiterentwicklung eines Programms für Molekülgraphik und Elektrondichte-Manipulation und seine Anwendung auf verschiedene Protein-Strukturaufklärungen. Ph.D. Thesis, Technische Universität, München.

Tsubouchi, H., and Ogawa, H. (1998). A novel mre11 mutation impairs processing of double-strand breaks of DNA during both mitosis and meiosis. Mol. Cell. Biol. *18*, 260–268.

Tsubouchi, H., and Ogawa, H. (2000). Exo1 roles for repair of DNA double-strand breaks and meiotic crossing over in Saccharomyces cerevisiae. Mol. Cell. Biol. *11*, 2221–2233.

Usui, T., Ohta, T., Oshiumi, H., Tomizawa, J., Ogawa, H., and Ogawa, T. (1998). Complex formation and functional versatility of Mre11 of budding yeast in recombination. Cell *95*, 705–716.

Varon, R., Vissinga, C., Platzer, M., Cerosaletti, K.M., Chrzanowska, K.H., Saar, K., Beckmann, G., Seemanova, E., Cooper, P.R., Nowak, N.J., et al. (1998). Nibrin, a novel DNA double-strand break repair protein, is mutated in Nijmegen breakage syndrome. Cell *93*, 467–476.

Ward, J.F. (1988). DNA damage produced by ionizing radiation in mammalian cells: identities, mechanisms of formation, and repairability. Prog. Nucleic Acid Res. Mol. Biol. *35*, 95–125.

Yamaguchi-Iwai, Y., Sonoda, E., Sasaki, M.S., Morrison, C., Haraguchi, T., Hiraoka, Y., Yamashita, Y.M., Yagi, T., Takata, M., Price, C., et al. (1999). Mre11 is essential for the maintenance of chromosomal DNA in vertebrate cells. EMBO J. *18*, 6619–6629.

Zdzienicka, M.Z. (1996). Mammalian X ray sensitive mutants: a tool for the elucidation of the cellular response to ionizing radiation. Cancer Surv. *28*, 281–293.

Accession Numbers

Coordinates for Mre11 (accession number 1II7) and the Rad50-ATPase (accession number 1II8) have been deposited in the Protein Data Bank.